Microwave-Plasma Interaction in a Miniature Plasma Ion Thruster

IEPC-2013-223

Presented at the 33rd International Electric Propulsion Conference,
The George Washington University • Washington, D.C. • USA
October 6 – 10, 2013

Indranuj Dey[1], Yuji Toyoda[2], Naoji Yamamoto[3] and Hideki Nakashima[4]
Department of Advanced Energy Engineering Science, Kyushu University, Kasuga, 816-8580, Japan

Abstract: A miniature microwave plasma source employing both radial and axial magnetic fields for plasma confinement has been developed for use as an ion thruster. The magnitude and phase of both the forward and reflected microwave power is measured to obtain the complex reflection coefficient from which the equivalent impedance of the plasma source is determined. The variation of the impedance coupled with a basic calculation model helps in understanding the physics behind the wave plasma interaction in the source.

Nomenclature

P_{in}	=	input (forward) power
P_{ref}	=	reflected power
F_t	=	thrust
I_{sp}	=	specific impulse
f_{in}	=	microwave input frequency
Q	=	mass flow rate
Γ	=	complex reflection coefficient
Z_L	=	equivalent configuration impedance
B_o	=	magnitude of magnetostatic field
V_S	=	screen voltage
V_A	=	acceleration voltage
I_b	=	extracted ion beam current
I_S	=	screen grid current
I_A	=	acceleration grid current
V_b	=	net ion beam voltage
Φ_Γ	=	reflection coefficient phase angle
Φ_Z	=	equivalent impedance phase angle
a	=	antenna radius
b	=	antenna enclosure radius
L	=	series inductance per unit length
G	=	shunt conductance per unit length
C	=	shunt capacitance per unit length
Z_{coax}	=	equivalent impedance of the coaxial sections
Z_{AT}	=	antenna impedance

[1] JSPS Researcher, indranuj@aees.kyushu-u.ac.jp, indranuj.dey@gmail.com.
[2] Master's Degree Student, toyoda@aees.kyushu-u.ac.jp.
[3] Associate Professor, yamamoto@aees.kyushu-u.ac.jp.
[4] Professor, nakasima@aees.kyushu-u.ac.jp.

I. Introduction

THE development and understanding of compact (discharge diameter < 30 mm), low power (P_{in} < 50 W) electric propulsion systems for orbit injection and attitude maintenance of Nano-satellites, and deep space propulsion of micro space probes is an active area of research.[1] Among the various electric thrusters currently operational, ion thrusters provide the highest efficiency and specific impulse.[2] Early ion thrusters employed DC discharges with filament cathodes for generation of plasma.[3] However, their lifetime was limited due to sputtering and contamination issues of the hot cathode and filament.[2,3] In order to circumvent the problem of limited lifetime, wave based plasma sources has been developed.[4-10] However, the research and development of wave based plasma sources in miniature configuration has been limited, with most of the work taking place in the RF regime,[7] or microwave surface wave regime.[8] Use of microwave induced electron cyclotron resonance (ECR) for plasma generation requires lower input power and propellant for operation, and hence are attractive choice for miniature plasma sources. A few researchers have attempted the development of microwave ECR sources in small geometries by employing various innovations to circumvent the geometrical cutoff problem associated with microwave propagation in waveguides.[9,10]

A miniature microwave ion thruster has been developed by Yamamoto et al. at Kyushu University,[9,11] having a F_t ~ 0.8 mN, and I_{sp} ~ 4100 s, for f_{in} = 2450 MHz, P_{in} ~ 8 W at xenon Q ~ 20 μg/s. The diameter of the discharge volume is 21 mm. The geometrical cutoff problem of microwaves is bypassed by launching the microwave via a Molybdenum antenna inside the discharge chamber. Since the microwave electric field mode established is evanescent, the ECR condition needs to be satisfied very near to the antenna for plasma ignition.[9-11] Research is in progress to enhance the performance of the ion thruster by modification of the magnetic field, antenna shape, change of boundary conditions, etc. Good thruster performance has been achieved using a combination of axial and radial magnetic field confinement, and proper frequency in the microwave regime. For the configuration used in this current experiment, typical thrust parameters obtained are, F_T ~ 0.74 mN, I_{sp} ~ 7588 s at P_{in} ~ 8 W with Q ~ 10 μg/s of Xe for the optimum frequency of 1600 MHz. The results are promising, and comparable to the output obtained in similar class of thrusters,[9-11] with a scope for further improvement. However, the nature of the interaction of the antenna launched microwave with the magnetically confined plasma is not well understood.

The small dimension of the plasma discharge volume presents formidable challenge for any in-situ electrostatic and electromagnetic measurements in the plasma. Even a non-invasive Laser Thomson Scattering diagnostic was performed under several limitations due to the problem of internal reflections and scattering in the small volume.[11] Therefore, investigation of microwave interaction with the magnetoplasma, has to be performed without intruding into the discharge volume. A non-invasive investigation is attempted in the current work and the results are presented in this article. The magnitude and phase of the forward and reflected microwave power into and out of the miniature plasma configuration is measured using heterodyne technique.[12] The measured quantities are used to determine Γ, from which Z_L can be determined. The variation of the magnitude and phase of Γ and Z_L under various input conditions is studied to gain an understanding of the microwave interaction with the compact magnetoplasma source. An attempt is made to develop an impedance model based on transmission line theory,[13] combined with antenna theory.[14] Explanation of the experimental observations with the model calculation would provide quantitative guidelines for future improvements in the thruster design.

The article is organized as follows: Section – II provides details of the ion thruster design, and gives the results of the ion beam extraction experiment. In Section – III, the reflection coefficient measurement experiment is described, and the results of the experiment are presented and discussed. Section – IV describes the formulation for the calculation of the thruster impedance, and the comparison of the theoretical results with experiments. The main results are discussed and future work is outlined in the conclusion in Section – V.

II. Ion Thruster Design and Ion Extraction

A. Ion thruster design

Fig. 1 shows the design schematic of the ion engine. It consists of a cylindrical aluminum discharge chamber (DC) of 21 mm inner diameter (CD). It is bounded by an aluminum back plate (BP) and a soft iron front plate (FP). The FP has a large 18 mm orifice which can be varied from 4 mm to 18 mm by attaching 1 mm thin stainless steel orifice plates if required. Eight stainless steel pipes containing bar magnets (BM) of dimension 15 mm × 5 mm × 5 mm surround the DC, and are held in position by two slotted rings (SR) of aluminum. The magnetization is along the radial direction, perpendicular to the DC axis. The BP has arrangement for attaching a microwave inlet (MI) feed through for attaching a linear molybdenum antenna (AT) of 1 mm diameter, and a gas inlet (GI) for introducing pure xenon gas into the DC. A soft iron block (SB) is attached to BP for axial containment of magnetic field lines, and

also acts as a ground plane for AT. A donut magnet (DM) with its magnetic field along the axis of the ion engine is attached on SB, coaxial with AT to provide an axial magnetic field. A two grid extractor system of carbon can be attached on the front plate with a screen grid (SG) at the same high positive potential as the ion thruster and an isolated acceleration grid (AG) held at a negative potential of few hundred volts for extraction of ions and prevention of electron back-streaming respectively.[2] There are 91 holes on the 0.3 mm thick grids, with SG hole diameter ~ 1.2 mm and AG hole diameter ~ 0.7 mm. The grids are separated by a distance of ~ 0.2 mm. The approximate beam diameter is 16 mm. The discharge chamber length CL (~ 22 mm) is measured between SB and SG, and can be varied by attaching additional aluminum or iron blocks on the SB. The total antenna length (AL ~ 20 mm) is measured from SB. The overall dimension of the ion thruster is ~ 50 mm × 50 mm × 50 mm.

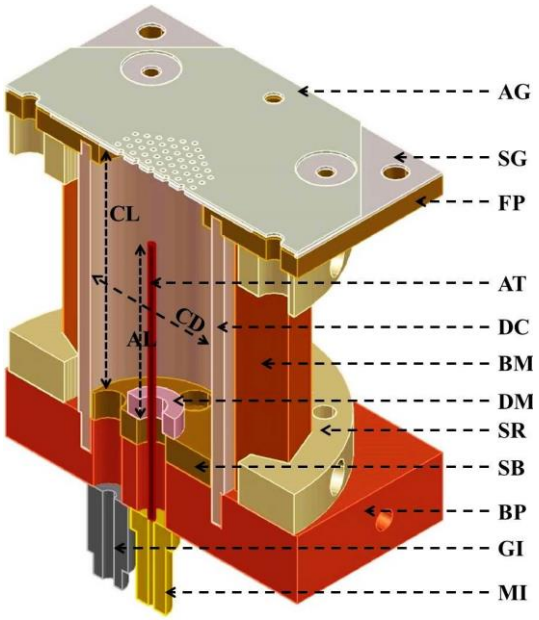

Figure 1. Design schematic of the ion thruster.

To have a uniform ground plane for the experiment, aluminum blocks AB are attached on the SB, concentric with DM (not shown in Fig. 1). Two such AB of different thicknesses is used to change the effective antenna length (AL_{eff}) and axial boundary (CL_{eff}), while maintaining a constant AL. The AL is kept unchanged to maintain a constant gap Δz ~ 2 mm between the tip of AT and SG, which was found to be optimum in earlier experiments.

B. Magnetic field map

The MAGNUM code of the AMAZE simulation suite is used to generate B_o contours and field lines in the radial and axial planes of the plasma source. Fig. 2 shows the magnetic field contours in the half axial plane. The other half is a mirror reflection by symmetry. The magnetization axis of the BM and DM are shown by bold arrows. The radial and the axial magnetic fields create the resultant B_o field as demonstrated. The ECR magnetic field values corresponding to the frequencies 1600 MHz ($\rightarrow$ 0.057 T) and 2450 MHz ($\rightarrow$ 0.086 T) are shown by slanted line and checkered pattern respectively. This plot provides an idea of the location of the ECR region with respect to the antenna. It is clearly observed that the ECR region for 1600 MHz has a broader spread while crossing AT, and is closer in proximity to it at other regions compared to the 2450 MHz condition. This makes 1600 MHz the optimum frequency for this configuration. The magnetic field lines (not shown) are predominantly axial near the antenna, and are radial towards the periphery. This is intended to reduce the electron diffusion towards the axial (back plane AB) and the radial boundaries, thereby enhancing the electron dwell time in the miniature configuration.

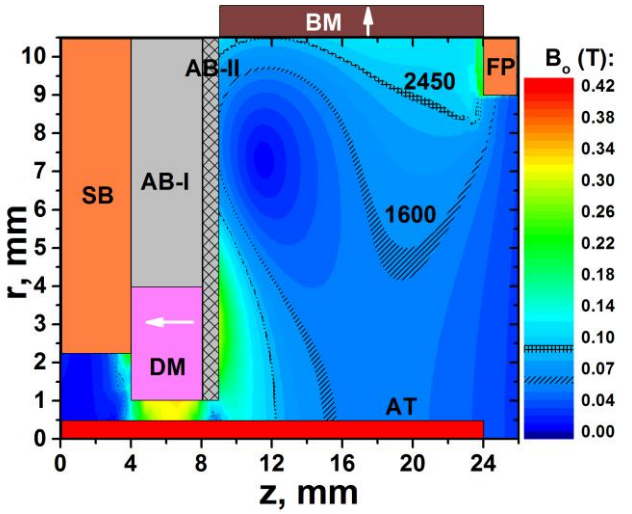

Figure 2. Contour plot of the magnitude of magnetic field in the axial plane.

Two configurations having different CL_{eff} and AL_{eff} are compared in this experiment. In the first configuration (Config. – I), the aluminum block (AB – I) is 4 mm in thickness, flush with DM (Fig. 2). This gives CL_{eff} ~ 18 mm, and AL_{eff} ~ 16 mm. In Config. – II, AB – II is 5 mm thick, enclosing the DM surface as shown in Fig. 2 by the cross patterned region. In this case CL_{eff} ~ 17 mm, AL_{eff} ~ 15 mm. In both cases, a Δz ~ 2 mm is maintained.

C. Ion extraction experiment

Fig. 3 shows the schematic of the ion beam extraction setup. The isolated ion thruster is placed inside a large vacuum chamber of diameter 60 cm and length of 100 cm, which is evacuated to a base pressure of 4×10^{-6} Torr by a Turbo-Molecular and Rotary pump combination. Pure xenon (99.999%) is used as the working gas, with the flow controlled by a Brooks 5850S thermal mass flow controller. Microwave power in the frequency range 800 – 1600 MHz is obtained from an Anritsu MG3660A (300 kHz-3000 MHz) signal generator (MXG) amplified by a solid-state amplifier (AMP). For 2450 MHz, a separate amplifier (MWG) is used. A DC block (DCB) isolates the thruster from the ground and also the microwave generator. A grounded aluminium mesh shields the thruster body from secondary electrons produced by the ion beam striking the inner wall of the vacuum chamber.

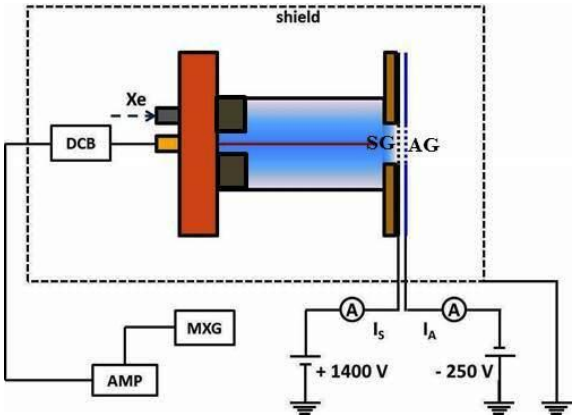

Figure 3. Setup for ion beam extraction.

The SG along with the thruster body is floated at V_S = +1400 V, and the AG is held at a potential of V_A = -250 V, with respect to vacuum chamber ground. Ion beam current is given by $I_b = I_S - I_A$. The I_S and I_A are converted to voltages separately, then digitized by a Yokogawa WE7000 module and recorded by a Personal Computer, along with P_{in} and gas mass flow rate.

The plot in Fig. 4 shows the variation of I_b with P_{in} at a mass flow rate of 10 μg/s, for f_{in} = 1600 and 2450 MHz and Config. – I and II. The current is observed to increase with P_{in}, with a slower growth rate at higher powers. The I_b at 1600 MHz is about 2 times higher than that at 2450 MHz for the same configuration, since the magnetic confinement is optimum for 1600 MHz. The faster saturation of I_b with P_{in} for 2450 MHz may be attributed to the fact that the highly energetic plasma electrons in ECR region have higher probability of being lost to the walls due to close proximity to the radial enclosing wall, thereby limiting their role in ionization. Therefore the increase in P_{in} does not appreciatively enhance the plasma density at 2450 MHz. For the 1600 MHz case, the degree of I_b saturation is much less, since the ECR region is away from the peripheral walls in most of the configuration (Fig. 2). In this case, the extracted ion beam is more likely to be space charge limited due to the perveance limit imposed by the grid system, rather than limitation due to plasma generation.

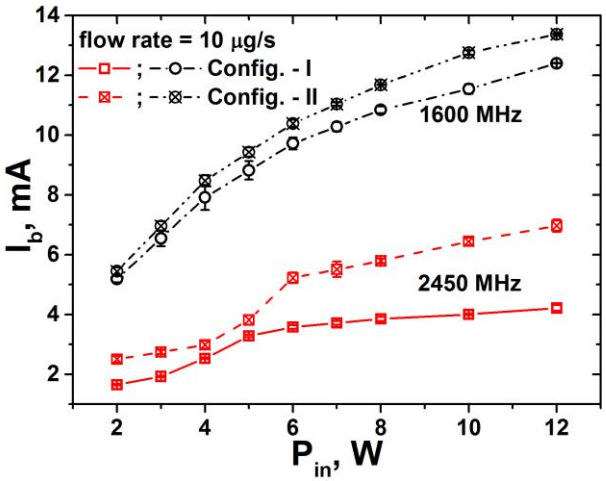

Figure 4. Variation of extracted ion beam current with input power.

The beam current is higher for Config. – II under same input conditions for both 1600 MHz and 2450 MHz. This due to the reduced CL_{eff} and AL_{eff}, which affects the input impedance of the thruster, discussed later in details. An I_b of 11.7 mA is obtained in Config. – II, for 1600 MHz, at a mass flow rate of 10 μg/s. Assuming $V_b = 0.9\left(V_S + |V_A|\right)$ ~ 1485 V, the thrust and specific impulse can be estimated using the relations,[2] $F_T = 1.65 I_b \sqrt{V_b}$ (mN) and $I_{sp} = 1.02 \times 10^5 \left(F_T / Q\right)$ (s) with Xe as the propellant, respectively. The calculated thrust parameters corresponding to the output are, F_T ~ 0.74 mN, and I_{sp} ~ 7588 s. For the 2450 MHz case (Config. – II), under the same input conditions, I_b ~ 5.8 mA, F_T ~ 0.37 mN, and I_{sp} ~ 3761 s.

III. Reflection Coefficient Measurement

Although, better thruster performance is obtained at 1600 MHz, reflection coefficient measurements are performed at 2450 MHz, due to signal generator and microwave amplifier constraints. It is assumed that the basic physical phenomenon involved, would remain the same and the experiments would nonetheless help in determining the important parameters influencing the interaction of the microwave with the magnetized plasma.

A. Measurement setup

Fig. 5 shows the experimental setup for the reflection coefficient measurement using the heterodyne technique. An Agilent 777 D (1900-4000 MHz) dual directional coupler (DDC) is attached to the 2450 MHz MWG. Two identical R&K – MX340-0S (1600-3600 MHz) mixers (MXC_1, MXC_2) are attached to the forward and reflected power coupled ports, with 30.1 dB mean directivity and 19.8 dB mean coupling at 2450 MHz. The MXG from the previous experiment acts as the local oscillator LO, and supplies a signal of 24495 MHz at 10 dBm to the mixers, resulting in an intermediate frequency of 500 kHz. The intermediate frequency carries the phase information of P_{in} and P_{ref} to and from the plasma, and is recorded by a Tektronix 2014 B digital storage oscilloscope (OSC). The $|P_{ref}|$ is separately measured by an Agilent E4418 B power meter (PM). The $|P_{in}|$ is obtained from the MWG, calibrated for the cable and connector losses. The DCB isolates the power and phase measurement from DC effects of the plasma. All the measuring instruments and components, including the OSC are connected by or terminated into 50 Ω lines and loads respectively, to avoid error due to impedance mismatch. The wave measurements are carried out in presence of the grids to maintain the same boundary condition and discharge pressure for the same Q as the ion beam experiment. However, the discharge chamber is grounded and the acceleration grid is kept floating, i.e., no ion beam current is extracted.

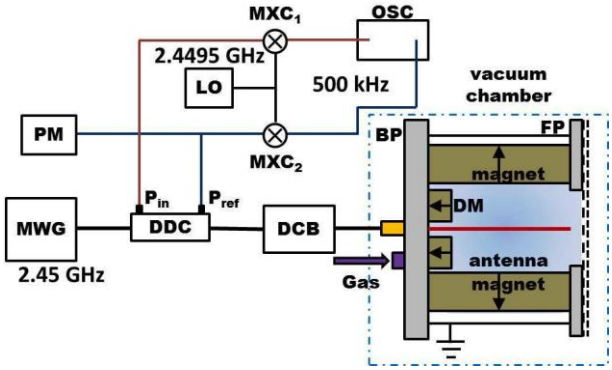

Figure 5. Reflection coefficient measurement setup.

In order to have an approximate idea of the variation in electron density in the source, a separate experiment is performed where the grids are replaced by an orifice of 6 mm diameter, and a circular planar probe of 5.5 mm diameter is placed just at the orifice exit edge to sample the plasma meniscus, so as to minimally effect the plasma inside. The probe is biased at +30 V to measure the electron current, proportional to the electron density inside the discharge chamber. The neutral transparency of the orifice-probe system is ~ 16%, which is higher than the equivalent grid transparency of 9% for the extraction experiment. It is assumed that this difference would not significantly affect the comparison.

Fig. 6 shows the variation of I_e with P_{in} for Config. – I and Config. - II, at Xe flow rates of 10 μg/s and 40 μg/s. The general trend of the variations is a slow rise at lower powers, followed by a faster rise, which again slows down at higher powers. The trend is qualitatively similar to the I_b variation (Fig. 4), with Config. – II showing a better performance. For a given configuration, the changes in slope of I_e are dictated by interaction between the microwave and the magnetized plasma surrounding the antenna. The fast increase in I_e signifies that the plasma density has crossed certain threshold value (which may be close to the O-mode cutoff density) resulting in resonant coupling of the microwave to the plasma electrons. As the power is further increased, the electrons gain higher kinetic energy and are lost easily in the compact configuration, thereby limiting their contribution to ionization. Hence, the increase in plasma density slows down. As explained earlier, for 2450 MHz, the ECR region lies close to the periphery, and hence the loss effect at higher powers is more prominent.

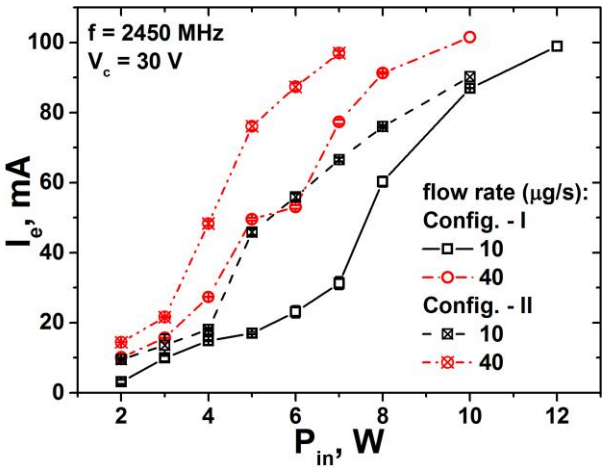

Figure 6. Experimental variation of electron current under various plasma conditions.

The magnitude of the reflection coefficient is obtained using the relation, $|\Gamma| = |P_{ref}|/|P_{in}|$. The downshifted forward and reflected signals recorded by the OSC are fitted in Origin 9.0 with a sinusoidal function of the form,

$$V_{IF} = V_{DC} + V_o \sin\{\pi(t - t_{ci})/w\}, \quad (1)$$

where, V_{IF} is the downshifted signal in volts, V_{DC} is the DC offset signal (~ 10^{-4} V), V_o is the oscillatory amplitude, t is time, t_{ci} is the epoch ($i = f, r$), and w is half the time period of the signal. The phase (Φ_{ci}) of the forward and the reflected waves are obtained from Eq. (1) as $\Phi_{ci} = \pi t_{ci}/w$. The phase difference corresponding to $|\Gamma|$ is given by $\Phi_\Gamma = \Phi_{cf} - \Phi_{cr}$. From the experimentally obtained $|\Gamma|$ and Φ_Γ, the complex reflection coefficient $\Gamma = |\Gamma|\exp(j\Phi_\Gamma)$ is obtained. From the knowledge of Γ, the complex impedance is obtained by,[13,14]

$$Z_L = 50(1+\Gamma)/(1-\Gamma), \tag{2}$$

which characterizes the wave interaction properties of the miniature magnetoplasma configuration.

To determine, whether the measurement setup is functioning properly and the calculation procedures are correct, the thruster is replaced by a 50 Ω matched termination, keeping all other cables and connectors the same. $|\Gamma|$ and Φ_Γ are obtained at various input powers. Fig. 7 shows the plot of the V_{IF} vs t for the matched termination condition at P_{in} = 8 W (red short dashed line). It can be easily seen that the reflected signal is out of phase by approximately π rad (180°) from the forward signal, thereby signifying reflection from a resistive load. The average magnitude and the phase of impedance are obtained as $|Z_L|$ = (47.4 ± 0.2) Ω, and Φ_Z = -(0.006 ± 0.002) rad respectively. This differs by about 5% from the ideal values of 50 Ω and 0.0 rad, and can be attributed to the frequency dependent VSWR, ageing, and wearing of the components and connectors. Subsequently, the same measurement is carried out with the thruster (Config. – I) under vacuum condition (no plasma). The V_{IF} plot in Fig. 6 (blue dash-dot line) clearly demonstrates the difference from the matched termination condition. The average $|Z_L|$ = (73 ± 1) Ω, and average Φ_Z = -(0.42 ± 0.02) rad, signifying that even in the absence of plasma, the discharge chamber impedance has a capacitive reactance component [Z_L = (67 – j29) Ω]. Similar results are obtained for Config. – II in vacuum viz., Z_L = (58 – j34.1) Ω, which has lower resistance but higher capacitance due to change in antenna and chamber length. In presence of plasma, the phase lies in between the matched termination and the vacuum case. A typical V_{IF} plot for Config. – I with Q = 10 μg/s and P_{in} = 8 W is shown in Fig. 6 (magenta dash-dot-dot line), with calculated Z_L = (40.0 – j2.8) Ω. Detailed experiments on the variation of the reflection coefficient with P_{in} for both the configurations at different Q values is carried out and analyzed. The results are discussed in the next subsection.

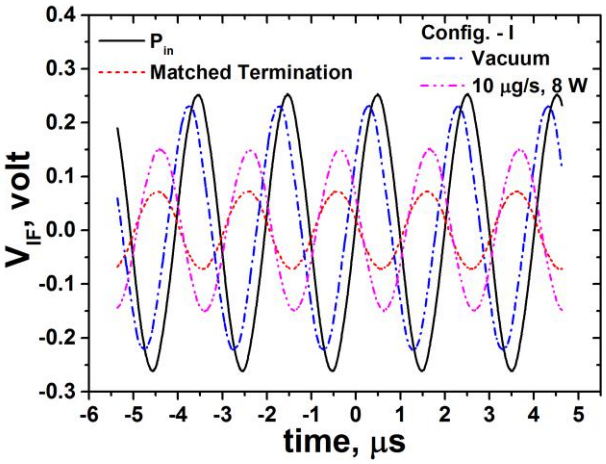

Figure 7. Experimental variation of intermediate frequency signal under various load conditions.

B. Reflection coefficient and impedance results

Fig. 8 (a) shows the variation of $|\Gamma|$ with P_{in} for the two thruster configurations, at Xe flow rates of 10 μg/s and 40 μg/s. In general, an increasing $|\Gamma|$ would indicate higher reflection from the load. It is observed from the plots that the variation of $|\Gamma|$ is different in nature for the Config. – I, Q = 10 μg/s case compared to the others. In this case, $|\Gamma|$ increases up to 6 W, and then decreases fast after 7 W, signifying that the plasma density crosses some critical value, around which the reflection is maximum. This is consistent with the I_e variation for the same condition in Fig. 6, where the current starts increasing fast after 7 W. For the other conditions, $|\Gamma|$ decreases fast for P_{in} > 3 W, signifying that, under these conditions, the plasma density has crossed the critical value at much lower power. The variation is again consistent with I_e variation in Fig. 6, where the faster slope takes over just after crossing P_{in} ~ 3-4 W. At higher powers (P_{in} > 8 W), there is a slight increase in $|\Gamma|$ (except for Config. – I, Q = 10 μg/s case) due to the insufficient utilization of input power for plasma growth owing to loss of energetic electrons as stated earlier.

The corresponding Φ_Γ vs P_{in} is plotted in Fig. 8 (b), below Fig. 8 (a), for the same input conditions. The phase difference values for Config. – I decreases from a higher value (> π rad) at lower P_{in}, towards π (~ 3.14 rad). For Config. – I, Q = 10 μg/s case, Φ_Γ goes down upto 3.5 rad, after which it increases to 3.6 rad. For Config. – I, Q = 40

μg/s case, Φ_Γ goes below π rad after 7 W, signifying change in the nature of reactance. For Config. – II, the Φ_Γ is always < π rad, with minimum occurring at 5 W and 4 W for Q = 10 μg/s, and 40 μg/s respectively.

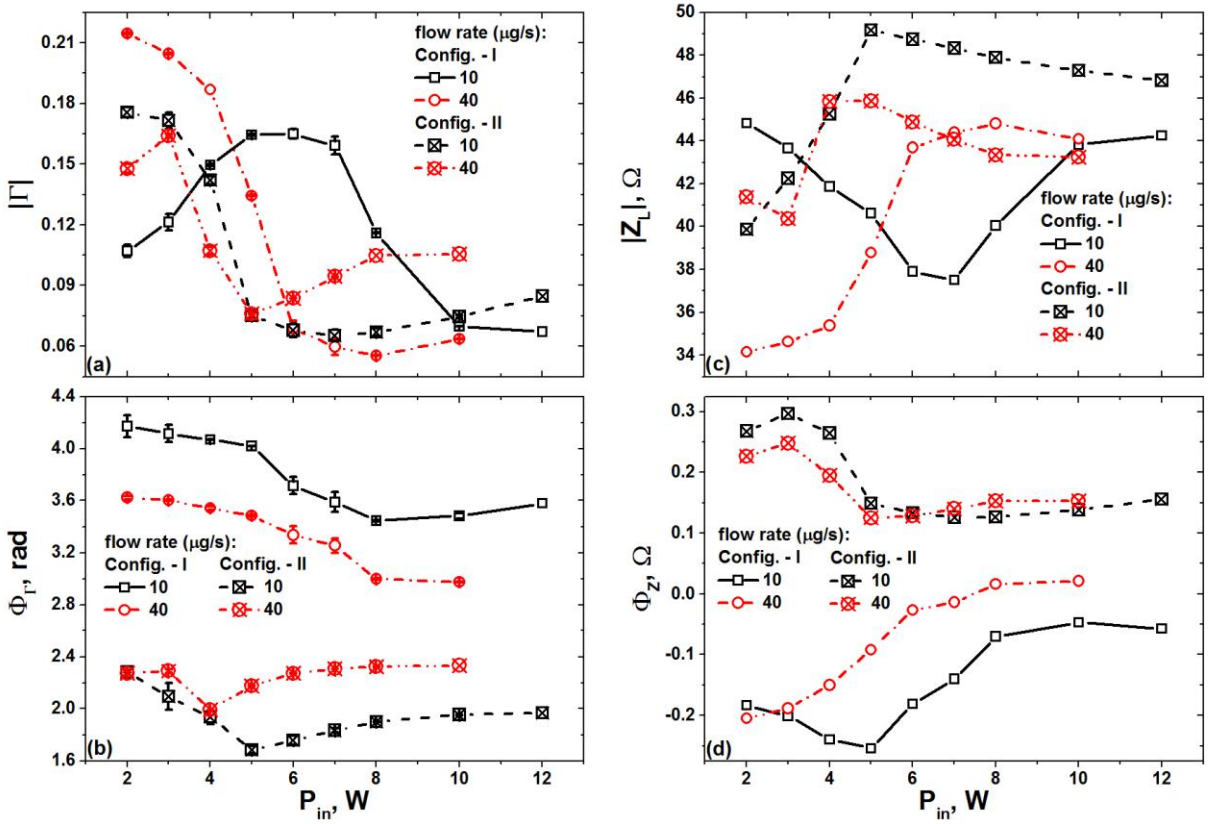

Figure 8. Experimental variation of, (a) |Γ|, (b) Φ_Γ, (c) $|Z_L|$, and (d) Φ_Z, with P_{in} under different input conditions.

To understand the experimental observations in terms of equivalent load impedance, the complex impedance (Z_L) is calculated from |Γ| and Φ_Γ, using Eq. (2). From Z_L, $|Z_L|$ and Φ_Z is obtained, which are plotted in Fig. 8 (c) and Fig. 8 (d) respectively. In the case of impedance, the efficiency of coupling of microwave power to a load is characterized by the difference of load impedance from the source impedance. In this experiment, the equivalent source impedance has been determined to be $|Z_L| \sim 47.4\ \Omega$ and $\Phi_Z \sim -0.006$ rad, from the matched termination data reported above (Fig. 7). Therefore, at lower Γ, $|Z_L|$ tends to be close to ~ 47 Ω, as observed in Fig. 8 (c). From Fig. 8 (d), it can be observed that the load reactance in Config. – I is predominantly capacitive ($\Phi_Z < 0.0$), and that in Config. – II is predominantly inductive ($\Phi_Z > 0.0$) at lower powers. At higher powers Φ_Z for both the configurations tend towards 0.0.

From the above experimental results and subsequent analysis, it is clear that an critical plasma density exists for the thruster configuration at 2450 MHz, crossing which results in the change of coupling mode of the microwave to the plasma. To determine the plasma density at which this transition takes place, a model calculation is attempted in the next section.

IV. Theoretical Impedance Calculation

In order to explain the experimental observations, and correlate the measured impedances with plasma electron density, an appropriate impedance calculation model is required. To account for the effects of the antenna and also the coaxial boundary surrounding it, a preliminary impedance model is developed using the transmission line theory for coaxial TEM line,[13] coupled with the theory of dipole antenna impedance,[14] modified for the current problem.

The various distinct sections of the configuration can be seen clearly from Fig. 2. For Config. – I, (1) SB (z_1 = 0-4 mm, $r_1 \sim 2.25$ mm); (2) DM (z_2 = 4-8 mm, $r_2 \sim 1.0$ mm); (3) DC (z_3 = 8-24 mm, $r_3 \sim 10.5$ mm); with $AL_I \sim 16$ mm.

The FP section is excluded, since the antenna terminates before entering it. For Config. – II, sections (1) and (2) remains the same, and a new section is introduced after (2), and the length of (3) and AL is shortened, viz., (2b) AB (z_{2b} = 8-9 mm, r_{2b} ~ 1.25 mm); (3) DC (z_3 = 9-24 mm, r_3 ~ 10.5 mm); and AL_{II} ~ 15 mm. In actual configuration, there is a very small gap between sections (2) and (2b) arising due to fabrication tolerances. There is also a region, preceding SB, in the BP where a boron nitride insulator is placed to protect the coaxial attachment from plasma. This region has an impedance different from the standard coaxial line impedance of 50 Ω, and will contribute to the calculated impedance. The region is designated as section 0 with r_0 ~ 2.25 mm.

The equivalent coaxial impedance (Z_{coax}) is evaluated from the equivalent *L*, *C*, and *G*, which in turn are calculated using the relations,

$$L = \sum_{i=0-3} \frac{\mu_o}{2\pi} \ln\left(\frac{r_i}{a}\right), \tag{3}$$

$$C = \sum_{i=0-3} \frac{2\pi\varepsilon_{re}}{\ln(r_i/a)}, \tag{4}$$

$$G = \sum_{i=0-3} \frac{2\pi\omega\varepsilon_{im}}{\ln(r_i/a)}, \tag{5}$$

where the summation is over all the sections. The series resistance per unit length is neglected, since all the sections involve conductors with very small resistivity. Here, $\omega = 2\pi f_{in}$, is the angular frequency. The real and imaginary dielectric permittivity are obtained from the complex permittivity, $\varepsilon_{plasma} = \varepsilon_{re} - j\varepsilon_{im} = \varepsilon_o\sqrt{K_{mag}}$, where K_{mag} is the relative dielectric in presence of magnetic field. K_{mag} is related to the plasma parameters by the relation,[14]

$$K_{mag} = 1 - \frac{\alpha_p^2 U}{U^2 - \beta_c^2}, \tag{6}$$

where $\alpha_p = \left(\sqrt{n_e e^2/m_e\varepsilon_o}\right)\Big/\omega$, $\beta_c = (eB_o/m_e)/\omega$, are the normalized plasma electron and electron cyclotron frequencies respectively, and n_e is the plasma electron density. The collisionality factor $U = 1 - j\nu_{coll}/\omega$, where the electron neutral collision frequency, $\nu_{coll} = 3.02\times10^{22} p_o K_{el}$, with elastic collision rate, K_{el} ~ 10^{-13} m^3/s and the neutral pressure p_o in Torr.[15] The fundamental constants ε_o (vacuum permittivity), *e* (electronic charge), and m_e (electron mass) have their standard values. The relative dielectric strength of boron nitride is 4.5, and is used in section 0 instead of K_{mag}. Using the calculated values of L, C, and G, the coaxial impedance can be calculated using,[13]

$$Z_{coax} = \sqrt{\frac{j\omega L}{G + j\omega C}}. \tag{7}$$

The pressure is estimated following the formulation in Ref. (16),

$$p_o = 4k_B T_g Q_o / v_g A_g, \tag{8}$$

where, T_g is the gas temperature (room ~ 298 K), $Q_o = 4.56\times10^{15} Q$ (atoms/s with *Q* in μg/s), v_g is the thermal velocity of the Xe atoms (~ 218 m/s at 298 K), and A_g is the effective transparent area of the grid of approximately 16 mm diameter (equivalent transparency ~ 9%). Plugging in the experimental parameters, the pressure at *Q* = 10 μg/s and 40 μg/s are 1.45 mTorr and 5.78 mTorr respectively.

The antenna impedance in presence of magnetized plasma for short dipoles, where the antenna length is much smaller than the wavelength is available in literature.[14] The same relation is applied to the current case of the monopole antenna by using the knowledge that, $Z_{monopole} = 0.5 Z_{dipole}$. The equivalent dipole length, corresponding to

the antenna in the current work, is about 4 times smaller than the wavelength corresponding to 2450 MHz in free-space. It is assumed that the short dipole approximation is valid in this case, and adequate for the intended preliminary estimates. The antenna impedance is given by,[14]

$$Z_{AT} = 0.5\{Z(\beta_V, AL_i) + Z(\beta_P, AL_i') - Z(\beta_S, AL_i)\}, \tag{9}$$

where, $Z(\beta_m, AL_i) = \dfrac{F(\beta_m)}{j\omega\pi\varepsilon_o AL_i}$. Here, m = vacuum (V), plasma (P), and plasma sheath (S), and i = I, II. The function $F(\beta_m)$ is expressed as,

$$F(\beta_m) = \ln\frac{\left(1+\sqrt{1+\beta_m^2}\right)^2}{\beta_m\left(2+\sqrt{4+\beta_m^2}\right)} + \frac{1}{2}\left[3\beta_m + \sqrt{4+\beta_m^2} - 4\sqrt{1+\beta_m^2}\right]. \tag{10}$$

The parameters $\beta_m = \beta_V, \beta_P$, and β_S, are given by, $\beta_V = a/AL_i$, $\beta_S = (a+d_s)/AL_i$, and $\beta_P = 0.5\beta_S\left(1+\sqrt{K_{mag}/K_o}\right)$ respectively. Here, the sheath thickness, $d_s = 5\times(\varepsilon_o T_e/en_e)^{1/2}$, with $T_e \sim 10$ eV. The modified antenna length is given by, $AL_i' = AL_i\sqrt{K_{mag}K_o}$, where $K_o = 1-\alpha_p^2/U$ is the relative dielectric corresponding to unmagnetized plasma.

The equivalent complex impedance for the thruster configuration is then given by,

$$Z_L = 1\Big/\left(\frac{1}{Z_{coax}} + \frac{1}{Z_{AT}}\right). \tag{11}$$

The limitation of this model is that the impedance has been estimated using expressions which have been derived for cold plasmas, with no spatial variation of plasma density or magnetostatic field. However, the experimental configuration has a strong radial and axial variation for both plasma density and magnetic field (Fig. 2). Also the presence of ECR region in the volume would also affect the impedance. For preliminary calculations, an average plasma density and an average magnetic field is assumed for the estimation of Z_L in the configuration.

First, the Z_L (and hence, $|Z_L|$ and Φ_Z) is calculated using the above formulation for the vacuum case ($n_e = 0$). The calculated values are compared with experimental results for vacuum in Table 1 below. It is observed that for Config. – I, the difference between experimental and theoretical values are $|\Delta Z_L| \sim 0.6\ \Omega$ and $|\Delta\Phi_Z| \sim 0.007$ rad, which is quite a good agreement. For Config. – II, $|\Delta Z_L| \sim 2.2\ \Omega$ and $|\Delta\Phi_Z| \sim 0.1572$ rad, the agreement is rather mediocre. The higher level of mismatch in Config. – II, especially in the phase value, can be attributed to the gap between the AB cover on the DM, where there is a finite gap due to fabrication tolerance. Also, there may be an error in the coaxial alignment due to the mechanical tolerance of the bolts attaching AB to BP via SB. In Config. – I similar tolerance error is expected, but the inner radius of the AB in this case does not influence the antenna, since it lies flush with the DM (Fig. 2). Overall, the agreement between the experimental and theoretical vacuum values of impedance is fair, and further calculations are carried out with model, in presence of plasma.

Table 1. Comparison of vacuum impedance values for the two configurations.

	Experiment		Theory	
	$\|Z_L\|$, Ω	Φ_Z, rad	$\|Z_L\|$, Ω	Φ_Z, rad
Config. – I	73.42	-0.4159	72.86	-0.4087
Config. – II	67.38	-0.5304	69.55	-0.3732

From previous research on ECR plasmas,[17] it is known that the plasma density in such sources are somewhere between 10^{15} m^{-3} to 10^{18} m^{-3}, depending on various factors like, neutral pressure, input power and extent of ECR region.[ref] The estimation of the average magnetic field is however more difficult in this case, and strongly depends on the region for average. Near the central region, in the radius range of 2-3 mm from the centre, the B_o varies from 0.05-0.1 T, over the whole axis (0-26 mm). Therefore, a theoretical plot of $|Z_L|$ and Φ_Z is obtained for various average magnetic fields for the plasma density range $n_e = 10^{15}$ m^{-3} to 10^{18} m^{-3} in Config. – I with Q = 10 μg/s, and is

shown in Fig. 9 (a) and Fig. 9 (b) respectively. It can be observed that the impedance is strongly influenced by the magnetic field values.

In Fig. 9 (a), the $|Z_L|$ plot for $B_o \leq 0.01$ T has only one peak at $n_e \sim 7.5 \times 10^{16}$ m^{-3}, which is very close to the critical density of the plasma ($\sim 7.44 \times 10^{16}$ m^{-3}). The peak signifies that the wave reflection increases as the density approaches this value. This peak is a common occurrence at all other B_o, except for the case of $B_o = 0.0875$ T, where there are no peaks. This is the ECR frequency and $|Z_L|$ is lower compared to other B_o values for the whole n_e range. A secondary peak comes into prominence at around 0.045 T (not shown). The peaks are well resolved at around 0.05 T, as shown in Fig. 9 (a). With increase in magnetic field the peak moves towards lower n_e, away from the critical density peak which also becomes smaller, as can be seen from the plot at 0.0825 T. The peaks disappear at 0.0875 T, and again reappear at 0.089 T on the higher side of n_e (> 10^{17} m^{-3}). The second peak grows in magnitude and moves towards the critical density peak upto 0.1 T [Fig. 9 (a)]. Above 0.125 T, the second peak moves back towards higher n_e, until it crosses 10^{18} m^{-3} at around 0.2 T. Variations above 0.1 T are not shown to avoid crowding of the plot in Fig. 9 (a). The primary peak is therefore controlled by the critical density, and the magnetic field mainly influences its magnitude. This peak can therefore be called the ordinary peak or O-peak. The secondary peak is influenced both by electron density and magnetic field, which strongly suggests that they are caused by the fulfillment of upper hybrid resonance (UHR) condition, viz., $\alpha_p^2 + \beta_c^2 = 1$, which is confirmed by calculations. This peak can therefore be called the extraordinary peak or the X-peak.

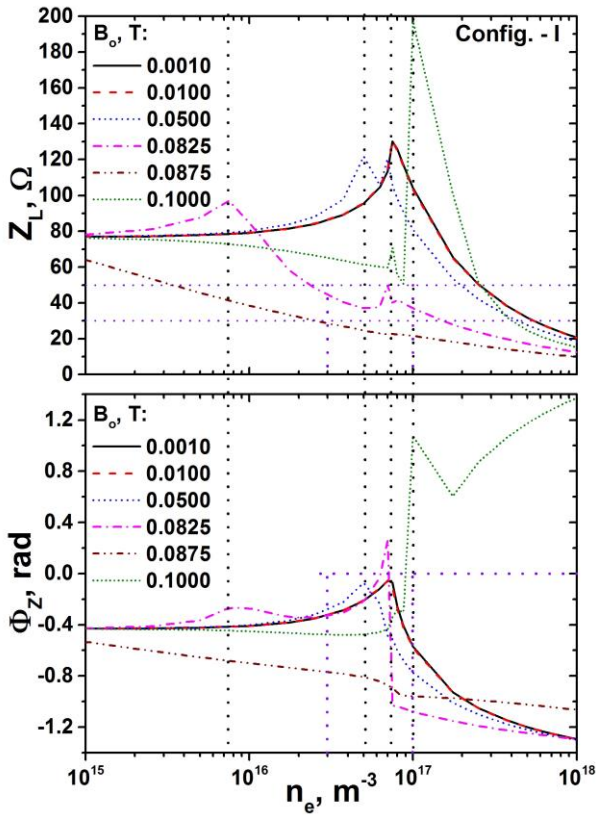

Figure 9. Theoretical variation of, (a) $|Z_L|$ and (b) Φ_Z, with n_e.

In Fig. 9 (b), the Φ_Z plot has a behavior similar to that of $|Z_L|$ variation in Fig. 9 (a). In many of the cases, a sharp drop or rise in the value of Φ_Z is observed in close proximity to the peaks, signifying a sharp change in the plasma-microwave coupling mode. Black dotted lines are drawn through the peaks in Fig. 9 (a) and dropped into Fig. 9 (b) to demonstrate the correlation between $|Z_L|$ and Φ_Z. For $B_o \sim 0.0825$ T, Φ_Z is seen to cross 0.0 rad near the O-peak density (critical density), and then again falling back to negative values, indicating the transition of capacitive coupling to inductive coupling, and again back to capacitive coupling. For 0.1 T, Φ_Z stays positive, i.e., in the inductive mode after the transition. This again shows that the magnetic field is extremely important in influencing the plasma-microwave interaction. From Fig. 9 (a), a region is identified, where 30 Ω < $|Z_L|$ < 50 Ω, which is the impedance range obtained from the experiments. The corresponding n_e is found to be between 3×10^{16} m^{-3} – 1×10^{17} m^{-3}, as shown by the violet dotted lines, and the range is used for further study. The B_o value is taken as 0.0825 T, close to the average value over a radius of 2.5 mm in the central region.

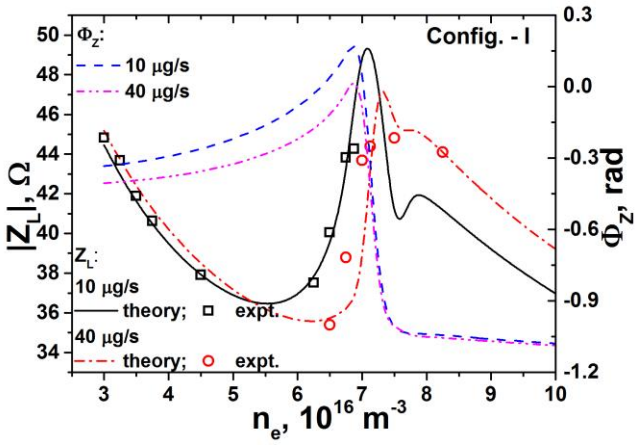

Figure 10. Variation of calculated $|Z_L|$ and Φ_Z, and experimental $|Z_L|$ with n_e in Config. – I.

Fig. 10 shows the n_e variation of $|Z_L|$ (left axis) and Φ_Z (right axis) for Config. – I at neutral pressures corresponding to Q = 10 and 40 μg/s. The effect of higher flow rate, and hence higher pressure is to reduce the sharpness of the peaks by increased

elastic electron-neutral collisions. An interesting feature is now observed for the O-peak, which is now more detailed due to the magnified scale. At Q = 10 μg/s, the peak region comprises of a maxima at ~ 7.0 × 10^{16} m^{-3}, followed by a minima at 7.4 × 10^{16} m^{-3}, again rising to a peak at 7.8 × 10^{16} m^{-3}. This is very similar to observations made in the study of small dipole antenna immersed in magnetized plasmas,[ref] where there is a sudden change from maxima to minima, as n_e approaches the critical density. The sharpness of the transition depends on the collisionality, and is damped at higher neutral pressures as observed for Q = 40 μg/s. The saddle like feature can be attributed to the joint influence of the sheath plasma and the bulk plasma, appearing as a difference term in Eq. (9), viz., $[Z(\beta_p,AL'_l) - Z(\beta_s,AL_l)]$. This also causes the slight shift of the peaks and magnitude variation with B_o, near the critical point.

In order to compare the theoretical variation with experimental values, the $|Z_L|$ data from Fig. 8 (c) has been superimposed on Fig. 10. Since, the independent axis of Fig. 8 (c) and fig. 10 are different (P_{in} and n_e respectively), the superposition has been done by matching the $|Z_L|$ value and the variation trend, with the guidance from I_e vs P_{in} variation in Fig. 6. The data points which do not match with the trend have been omitted. It is observed that the experimental $|Z_L|$ values for Q = 10 μg/s agrees very well with the theoretical variation. For the Q = 40 μg/s case, the agreement is good at higher densities. The trend of the Φ_Z variation matches well with the experiment, though there is a difference in the values.

In Fig. 11, the n_e variation of $|Z_L|$ (left axis) and Φ_Z (right axis) for Config. – II is shown, at neutral pressures corresponding to Q = 10 and 40 μg/s. The $|Z_L|$ peak occurs at 7.4 × 10^{16} m^{-3} in this case, with the minima around 7.8 × 10^{16} m^{-3}. The second maxima is flattened out and occurs at ~ 9.7 × 10^{16} m^{-3} for 10 μg/s and at ~ 8.8 × 10^{16} m^{-3} for 40 μg/s. In this case, the minima is seen to be deeper compared to Config. – I. The $|Z_L|$ experimental data has partial agreement with the theoretical values in this case. The Φ_Z variation also has qualitative agreement with the experimental results, with the values being positive (inductive mode) for n_e > 7.4 × 10^{16} m^{-3}. The mediocre correlation between the experiment and theory in this case are attributable to the mechanical deficiencies during assembling of the configuration, as explained earlier.

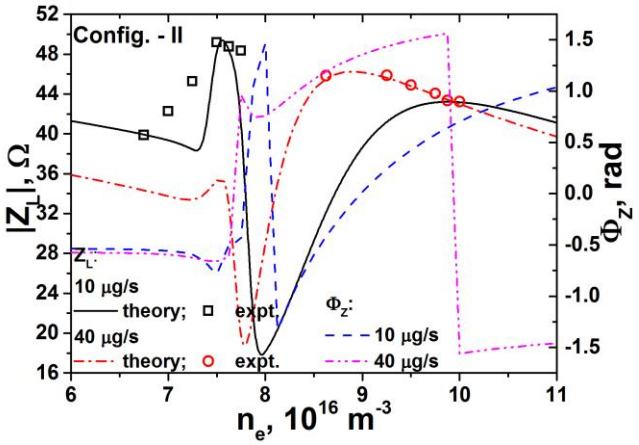

Figure 11. Variation of calculated $|Z_L|$ and Φ_Z, and experimental $|Z_L|$ with n_e in Config. – II

The developed model though limited to uniform plasmas, provides a basic understanding of the interaction between the antenna launched microwave and the magnetoplasma in the compact configuration. The calculation procedure establishes the basic framework on basis of which further developments can be carried out. Several improvements are in the pipeline to make the model more realistic and closer to the experimental conditions. This includes the re-derivation of the impedance relations, taking into account the spatial variation of the plasma density and magnetic field. Also the effect of the FP boundary (grids) would be included, which has been neglected here.

V. Conclusion

A compact microwave ECR plasma source has been developed and implemented as an ion thruster for space propulsion applications. Ion beam extraction experiments have been performed on the thruster, where two closely related boundary configurations have been compared. Typical thrust parameters obtained are, F_T ~ 0.74 mN, I_{sp} ~ 7588 s at P_{in} ~ 8 W with Q ~ 10 μg/s of Xe for the optimum frequency of 1600 MHz. To understand the physics of the wave interaction with the compact magnetoplasma, a reflection coefficient experiment has been conducted using the heterodyne technique at 2450 MHz. The complex impedance characterizing the wave response of the plasma source has been calculated from the complex reflection coefficient. Interesting results indicating the existence of distinct coupling modes across a critical plasma condition has been observed. A basic impedance model is developed by combining transmission line theory for coaxial cables with the theory for small antennas immersed in magnetized plasma. The theory and the experiment demonstrate fair qualitative agreement and a partial quantitative agreement. The critical plasma condition is found to overlap with the critical plasma density where the plasma frequency matches the input frequency, above which the plasma is overdense with respect to the microwave frequency.

The results obtained from this study would help to design future thruster configurations. Several, improvements can be made to the existing thruster also, based on the study. Efforts towards designing and fabricating a better and more coaxial aluminum block for Config. – II is expected to reduce the mismatch, and help in better coupling of the microwave power to the magnetized plasma. Future studies with 1600 MHz, and other propellants (Krypton, Argon) are also planned to study the effect of frequency and ionization potential on the reflection coefficient.

Acknowledgments

The authors acknowledge the Japan Society for Promotion of Sciences (JSPS) for the Grant-in-Aid for research (Grant No.: 23・01379). I. Dey would like to acknowledge the JSPS for the Postdoctoral Scholarship for Foreign Researchers.

References

[1]Blaney, D. L., Staehle, R. L., Betts, B., Friedman, L., Hemmati, H., Lo, M., et al. "Interplanetary cubesats: Small, low cost missions beyond low Earth orbit." *Lunar and Planetary Institute Science Conference Abstracts*, 1868, Vol. 43, LPI, The Woodlands, Texas, 2012.

[2]Goebel, D. M., and Katz, I., . *Fundamentals of electric propulsion: ion and Hall thrusters*, Wiley, New Jersey, 2008, pp. 4, 22, 25, 192..

[3]Kaufman, H. R., "Technology of Electron-Bombardment Ion Thrusters", *Advances in Electronics and Electron Physics*, Vol. 36, 1975, pp. 265-373.

[4]Divergilio, W. F.,Goede, H., and Fosnight, V. V., "High Frequency Plasma Generators for Ion Thrusters", #CR-167957, NASA, 1981.

[5]Kuninaka, H., and Satori, S., "Development and Demonstration of a Cathode-less Electron Cyclotron Resonance Ion Thruster", *Journal of Propulsion and Power*, Vol. 14, 1998, pp. 1022-1026.

[6]Charles, C., Boswell, R. W., and Lieberman, M. A., "Xenon ion beam characterization in a helicon double layer thruster", *Applied Physics Letters*, Vol. 89, 2006, 261503.

[7]Charles, C., and Boswell, R. W., "Measurement and modelling of a radiofrequency micro-thruster", *Plasma Sources Science and Technology*, Vol. 21, 2012, 022002.

[8]Takahashi, T., Takao, Y., Eriguchi, K., and Ono, K., "Numerical and Experimental Study of Microwave-Excited Microplasma and Micronozzle Flow for a Microplasma Thruster", Physics of Plasmas, Vol. 16, 2009, 083505.

[9]Yamamoto, N., Kondo, S., Chikaoka, T., Nakashima, H., and Masui, H.,. "Effects of Magnetic Field Configuration on Thrust Performance in a Miniature Microwave Discharge Ion Thruster", *Journal of Applied Physics*, Vol. 102, 2007, 123304.

[10]Koizumi, H., and Kuninaka, H., "Miniature Microwave Discharge Ion Thruster Driven by 1 Watt Microwave Power", *Journal of Propulsion and Power, Vol.* 26, 2010, p. 601.

[11]Yamamoto, N., Tomita, K., Yamasaki, N., Tsuru, T., Ezaki, T., Kotani, Y., Uchino, K., and Nakashima, H., "Measurements of Electron Density and Temperature in a Miniature Microwave Discharge Ion Thruster Using Laser Thomson Scattering Technique", *Plasma Sources Science and Technology*, Vol. 19, 2010, 045009.

[12]Eom, G. S., Kwon, G. C., Bae, I. D., Cho, G., and Choe, W., "Heterodyne Wave Number Measurement Using a Double B-dot Probe", *Review of Scientific Instruments*, Vol. 72, 2001, pp. 410-412.

[13]Pozar, D. M., *Microwave Engineering*, 3rd Ed., Wiley, New Jersey, 2005, pp. 52-54.

[14]Blackwell, D. D., Walker, D. N., Messer, S. J., and W. E. Amatucci, "Antenna Impedance Measurements in Magnetized Plasma. II. Dipole Antenna" *Physics of Plasmas*, Vol. 14, 2007, 092106.

[15]Lieberman, M. A., and Lichtenberg, A. J., Principles of Plasma Discharges and materials Processing, 2nd Ed., Wiley, New Jersey, 2005, pp. 78-80.

[16]Chabert, P., Monreal, J. A., Bredin, J., Popelier, L., and Aanesland, A., "Global Model of a Gridded-ion Thruster Powered by a Radiofrequency Inductive Coil", *Physics of Plasmas*, Vol. 19, 2012, 073512.

[17]Moisan, M., Pelletier, J., Microwave Excited Plasmas, Elsevier, Amsterdam, 1992, pp. 392-394.